Solar Gasification of Carbonaceous Waste Feedstocks in a Packed-Bed Reactor—Dynamic Modeling and Experimental Validation

Nicolas Piatkowski
ETH Zurich, Department of Mechanical and Process Engineering, 8092 Zurich, Switzerland

Aldo Steinfeld
Dept. of Mechanical and Process Engineering, ETH Zurich, 8092 Zurich, Switzerland

Solar Technology Laboratory, Paul Scherrer Institute, 5232 Villigen PSI, Switzerland

DOI 10.1002/aic.12545
Published online February 28, 2011 in Wiley Online Library (wileyonlinelibrary.com).

Thermochemical gasification of carbonaceous waste feedstocks (specifically: scrap tire powder, industrial sludge, and sewage sludge) for high-quality syngas production is numerically modeled and experimentally validated using concentrated solar process heat. The solar reactor consists of two cavities separated by a radiant emitter, with the upper one serving as the solar radiative absorber and the lower one containing the reacting packed bed. The reactor is modeled by considering combined heat transfer coupled to the reaction kinetics, driven by the applied solar flux at the reactor's aperture. Model validation is accomplished in terms of converted mass, reactor temperatures, efficiency, and solar upgrade based on experiments with an 8-kW reactor subjected to solar fluxes up to 2560 suns and packed bed temperatures up to 1490 K. The transient operation of a 200-kW pilot-scale reactor for gasifying industrial sludge is simulated for a solar day, yielding a maximum solar-to-fuel energy conversion efficiency of 89%. © 2011 American Institute of Chemical Engineers *AIChE J,* 57: 3522–3533, 2011
Keywords: gasification, carbonaceous, coal, biomass, syngas, solar, energy, heat transfer, reactor, packed bed, simulation, mathematical modeling, thermochemistry

Introduction

The thermochemical production of solar fuels uses concentrated solar energy to deliver high-temperature process heat to drive endothermic chemical reactions.[1] Of special interest is the steam-based gasification of carbonaceous feedstocks such as coal, biomass, or carbon-containing wastes,[2] which produces high-quality synthesis gas (syngas)—mainly H_2 and CO—applicable for power generation in combined cycles and fuel cells, or for Fischer-Tropsch processing to liquid fuels. Conventional autothermal gasification requires a portion of the injected feedstock mass to be combusted to supply the required process heat. To improve burn efficiency and avoid contamination by NO_x, high purity O_2 (typically 95%) stemming from cryogenic air separation must be supplied. This process is particularly energy intensive, requiring 200 kWh/ton, thus, representing about 20% of total plant cost and 15% of the gross power of the plant.[3] Considering the energy balance, 12 MJ/kg are required to steam-gasify a typical bituminous coal of LHV 34 MJ/kg.[4] Therefore, in autothermal operation, about 35% of the injected coal mass must be burned uniquely to power the reaction, which inherently decreases coal utilization and contaminates the product gases with combustion products. Motivated by the combined

Correspondence concerning this article should be addressed to A. Steinfeld at aldo.steinfeld@ethz.ch.

benefits of waste management and fuel recovery, carbonaceous waste gasification has been investigated in the laboratory and modern waste-to-energy systems,[5–8] where the combustion products were separated from the product gas and discharged to the environment. For a variety of carbonaceous wastes, experiments showed 75% to 85% of the introduced feedstock's energy content being captured in the syngas.[6]

In contrast, solar-driven gasification is free of pollutants and/or combustion byproducts. The product syngas has a lower CO_2 intensity because its calorific value is solar-upgraded over that of the original feedstock by an amount equal to the enthalpy change of the endothermic reaction. Based on the stoichiometric gasification of pure carbon, the LHV of the syngas product is 33% higher than that of the original carbon. A second law (energy) analysis indicated that Brayton-Rankine combined power cycles running on solar-made syngas from coal can double the specific electric output per unit mass of coal and, consequently, avoid half the specific CO_2 emissions of conventional coal-fired generation plants.[4] In the long term, this technology has the potential of becoming economically competitive even before the application of government subsidies and/or credit for pollution abatement, mainly due to the elimination of the air separation unit as well as significant savings (>35%) in feedstock consumption.[9]

The solar gasification of petroleum coke and coal was performed in fluidized-bed and vortex-flow solar reactors,[1,4,10–14] where the direct irradiation of particle suspensions was found to be an effective means of heat transfer directly to the reaction site, producing ultra fast heating rates (~1000 K/s) and enhanced kinetics.[14] The transparent window needed for optical access of concentrated solar radiation is, however, a critical component under high pressures and severe atmospheres. The large volume flow rates of inert carrier gas or excess steam necessary for fluidization and for protecting the window displace syngas, decreasing production and energy conversion efficiency.[15] Effective fluidization also requires small particle sizes (<5 mm) and narrow particle size distributions, making particle suspension reactors poorly adapted to highly variable and heterogeneous feedstocks such as wastes and more costly due to necessary extra feedstock handling operations such as milling, sifting, and drying.[15] Indirectly irradiated reactors eliminate the need for a window at the expense of having less efficient heat transfer—by conduction—through the walls of an opaque absorber. The disadvantages are linked to the limitations imposed by the materials of the absorber, with regards to maximum operating temperature, inertness to the chemical reaction, thermal conductivity, radiative absorptance, and resistance to thermal shocks. Exploratory studies with packed bed reactors investigated solar gasification of feedstocks such as coal, oil shale, biomass, scrap tire, and polyethylene wastes, and the carbothermal reduction of electric arc furnace dusts.[16–18] Recently, solar gasification of carbonaceous feedstocks including wastes was experimentally studied and demonstrated in an indirectly irradiated packed-bed reactor.[19] These studies showed the reactor concept to be robust for these highly variable feedstocks, producing high-quality syngas in all cases. Similarly, gasification of sewage sludge in a radiation-driven batch reactor was investigated.[20] In this context, solar gasification should be viewed as a viable waste management and fuel recovery option with the additional benefit of the chemical storage of solar energy.

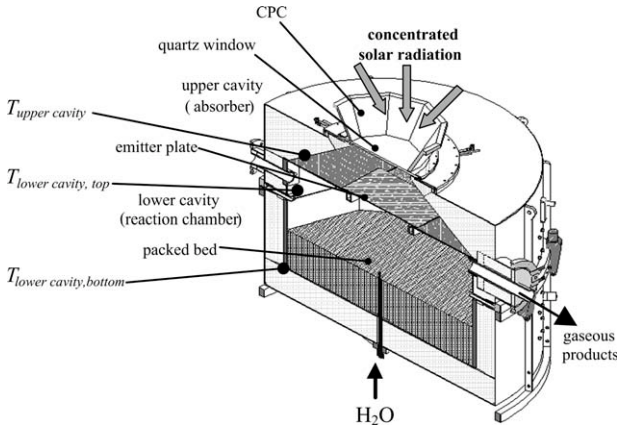

Figure 1. Schematic of the packed-bed solar reactor, featuring two cavities separated by an emitter plate, with the upper one serving as the radiative absorber and the lower one containing the reacting packed bed that shrinks as the reaction progresses.

Numerical studies performed in the area of packed-bed solar reactors have considered the thermochemical decomposition of $CaCO_3$, carbothermal reduction of ZnO, and the steam-gasification of charcoal.[21–23] The packed beds underwent rapid heating on the irradiated surfaces, but as is typical of ablation regimes, heat transfer through the porous bed was found to be the reaction limiting factor.[21,23,24] At above 1300 K, the predominant heat transfer mode in the bed was radiation, producing a seven-fold increase in packed effective bed thermal conductivity.[21,23]

This paper presents the design, experimentation, and dynamic modeling of a solar packed-bed reactor for the steam gasification of highly heterogeneous waste carbonaceous feedstocks. The driving boundary condition is the applied solar flux at the reactor's aperture, making the model readily applicable to dynamic simulations under real transient solar irradiation. The unsteady state governing energy equations and associated boundary conditions are formulated for the model and solved numerically. The model is validated on the basis of reactor temperatures, converted mass, energy conversion efficiency, and solar upgrade with experimental results of waste gasification previously obtained using a 8-kW solar reactor prototype tested in a high-flux solar simulator.[19] Finally, the model is used to assess the performance of a 200-kW solar-driven packed bed gasifier.

Solar Reactor Configuration

The solar reactor is schematically shown in Figure 1. Its design and associated experimental setup have been previously described in detail[19]; only the main features are highlighted here. It is specifically designed for a "beam-down" (Cassegrain) optical configuration of solar towers.[25] The reactor consists of two cavities in series. The upper cavity functions as the solar absorber and contains a windowed aperture to let in concentrated solar radiation. The lower cavity

Table 1. Ultimate and Proximate Analyses and Packed Bed Properties of Carbonaceous Waste Feedstocks Considered for Steam Gasification

Feedstock	Scrap Tire Powder	Industrial Sludge	Sewage Sludge
Ultimate Analysis			
C (wt %)	82.20	67.48	51.39
H (wt %)	7.30	8.94	7.59
O (wt %)	3.60	22.60	32.81
N (wt %)	0.39	0.91	6.64
S (wt %)	1.90	0.44	1.57
Proximate Analysis			
Ash (wt %)	4.5	19.9	33.5
Volatile (wt %)	67.5	62.2	51.9
Water (wt %)	1.0	5.5	7.2
C-fix (wt %)	27.0	12.4	7.4
$LHV_{feedstock}$ (kJ/kg)	35,515	19,305	10,288
Bed Physical Properties			
Particle size range (mm)	0.1–2	10–30	0.1–3
Particle form	Regular particles	Irregular chunks	Regular particles
ρ_{eff} (kg/m^3)	380	440	770
Bed porosity	0.3	0.4	0.3

functions as the reaction chamber and contains the shrinking packed bed on top of the steam injector. A SiC emitter plate separates the two cavities and acts as solar absorber and radiant emitter. Its main purpose is to protect the window from deposition of particles or condensable gases. A nonimaging compound parabolic concentrator (CPC)[26] is incorporated at the aperture to augment the solar concentration ratio and reduce reradiation losses. The reactor is operated in batch mode, with the packed bed shrinking as the gasification reaction progresses, necessitating a dynamic modeling treatment.

An 8-kW reactor prototype was fabricated with an upper cavity containing a 6.5-cm diameter aperture and a 14.3-cm diameter, 16-cm height lower cylindrical cavity. The 6-mm-thick emitter plate was made of SiC-coated graphite. The upper cavity was sealed by a 3-mm-thick fused quartz window located at the aperture and mounted in a water-cooled gasket. The upper cavity was also purged with a 2 L/min N_2 flow. The lower cavity was lined with 6-mm-thick SiC tiles and with 70-mm-thick Al_2O_3-SiO_2 insulation. A steam-argon mixture with liquid water flow rates up to 8 ml/min and an Ar flow rate of 2 l_N/min* was introduced from below the packed bed. Product gases exited through a lateral outlet port and were analyzed by gas chromatography. Key temperatures were measured at the top $T_{\text{lower cavity,top}}$ and bottom $T_{\text{lower cavity,bottom}}$ of the lower cavity with type-K thermocouples, and at the surface of the insulation cone $T_{\text{upper cavity}}$ with a type-S thermocouple, as indicated in Figure 1. The experiments were carried out at PSIs high-flux solar simulator (HFSS).[27] Radiative fluxes incident into the reactor were measured optically with a calibrated CCD camera on a water-cooled Lambertian target and verified with a water-cooled calorimeter. The maximum radiative flux at the reactor's aperture was equivalent to a solar concentration ratio of 2560 suns (1 sun = 1 kW/m^2).

Feedstocks

Three waste feedstocks were used to validate the reactor model: scrap tire powder, industrial sludge (a mixture of paints, dyes, inks, and solvents), and dewatered sewage sludge. The characteristics of these materials vary greatly in terms of physical and thermal properties as well as proximate and ultimate analyses as shown in Table 1. Of particular note are the large volatile fractions making pyrolytic reactions of principle importance.[28] Variations in particle size, bed porosity, and packed bed effective density were considered for scrap tire powder in the gasification regime and influenced the packed bed dynamics.[29] For the other materials, constant particle sizes, porosities, and densities were considered.

The gasification process is represented by the simplified net stochiometric reaction:

$$C_1H_xO_yS_uN_v + (1-y)H_2O = \left[\frac{x}{2} + 1 - y - u\right]H_2 + CO + uH_2S + \frac{v}{2}N_2 \quad (1)$$

The specific reaction enthalpy change Δh_{chem}, shown in Figure 2 for the three feedstocks, was determined from the equilibrium composition of the carbonaceous feedstock-steam system at T_{bed}.[4,21] The reaction enthalpies of pyrolytic reactions were neglected due to the huge uncertainty in their determination and their low value compared with those for gasification.[30]

Solar Reactor Model

Three regions of interest were modeled: (1) the upper cavity, which receives concentrated solar radiation as the boundary condition, (2) the lower cavity, which contains the reacting packed bed, and (3) the reactor insulation.

Upper cavity model

Figure 3a depicts the heat and mass flows affecting the upper cavity of the reactor. Concentrated solar radiative flux q_{solar} arriving at the external surface of the window serves as the driving boundary condition. Because of the CPC placed at the aperture, q_{solar} can be considered diffuse. Diffuse radiative flux $q_{\text{emitter,lower cavity}}$ is also emitted to the lower cavity from the emitter plate ring elements facing the lower cavity. The insulation cone participates through the conductive flux $q_{\text{inscone,ins}}$. An Ar purge gas flow of not more than 2 l_N/min

*l_N means liters at normal conditions; mass flow rates are calculated at 273 K and 1 bar.

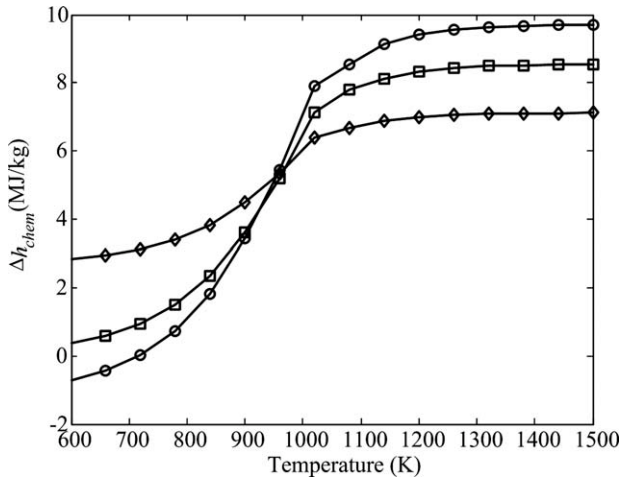

Figure 2. Specific enthalpy change Δh_{chem} of the steam gasification of the carbonaceous waste material (Eq. 1) as a function of temperature *T*, with the reactants and products both at temperature *T*, and the products having the equilibrium composition.

Legend: ◇, sewage sludge; □, industrial sludge; ○, tire powder.

is injected into the upper cavity at the "cold surface"—a 16 mm water-cooled gap between the insulation cone and the plane of the window—and exits via the space between the insulation cone and the emitter plate.

The radiative exchange within the upper cavity was solved by applying the radiosity formulation for an enclosure with N isothermal surfaces, as shown in Figure 3b: one window, one cold surface, N_{emitter} concentric rings of the emitter plate, and N_{inscone} conical ring surfaces. The spectrally selective quartz window S1 was modeled as a semitransparent disk using the semigray band approximation over three spectral bands with hemispherical emittance E, transmittance V, and reflectance R listed in Table 2.[31,32] The window increases reflection losses of directly incident solar radiation, but decreases long wave radiation losses compared with a windowless cavity.[33]

The net radiative flux on each surface k of the upper cavity for each spectral band b is given by[34]

$$q_{k,b} = q_{o,k,b} - q_{i,k,b} + q_{l,k,b} - q_{e,k,b} \tag{2}$$

The first two terms of Eq. 2, radiosity and incident fluxes, are applicable to all surfaces while the last two—externally leaving and applied fluxes—only to semitransparent surfaces. $q_{o,k,b}$ is the spectral radiosity flux from surface k directed towards the inside of the enclosure and is given by:

$$q_{o,k,b} = \text{FF}_{b,\lambda T_k} E_{k,b} \sigma T_k^4 + \text{FF}_{b,\lambda T_{\text{solar}}} V_{\text{k,b}} q_{\text{e},k} + R_{k,b} q_{i,k,b} \tag{3}$$

where $\text{FF}_{b,\lambda T_k}$ is the fractional function in spectral band b for radiation originating from a surface at temperature T_k, analytically determined using the series expansion.[34] $q_{e,k}$ is the externally supplied flux to surface k and is equal to q_{solar} for the window S1. The last term of Eq. 3 is the reflection of incident flux arriving at surface k from within the enclosure, given by:

$$q_{i,k,b} = \sum_{j=1}^{N} q_{o,j,b} F_{k-j} \tag{4}$$

where $F_{k\text{-}j}$ is the view factor from surface k to surface j and $q_{o,j,b}$ is the radiosity flux from surface j in spectral band b, which arrives at surface k. The view factors for all surfaces $F_{k\text{-}j}$ were computed by Monte-Carlo ray tracing. Equations 3 and 4 are coupled and must be solved iteratively until $|1 - q_{i,k,b}^{\text{new}}/q_{i,k,b}^{\text{old}}| \leq 10^{-4}$ with superscripts *new* and *old* representing values of

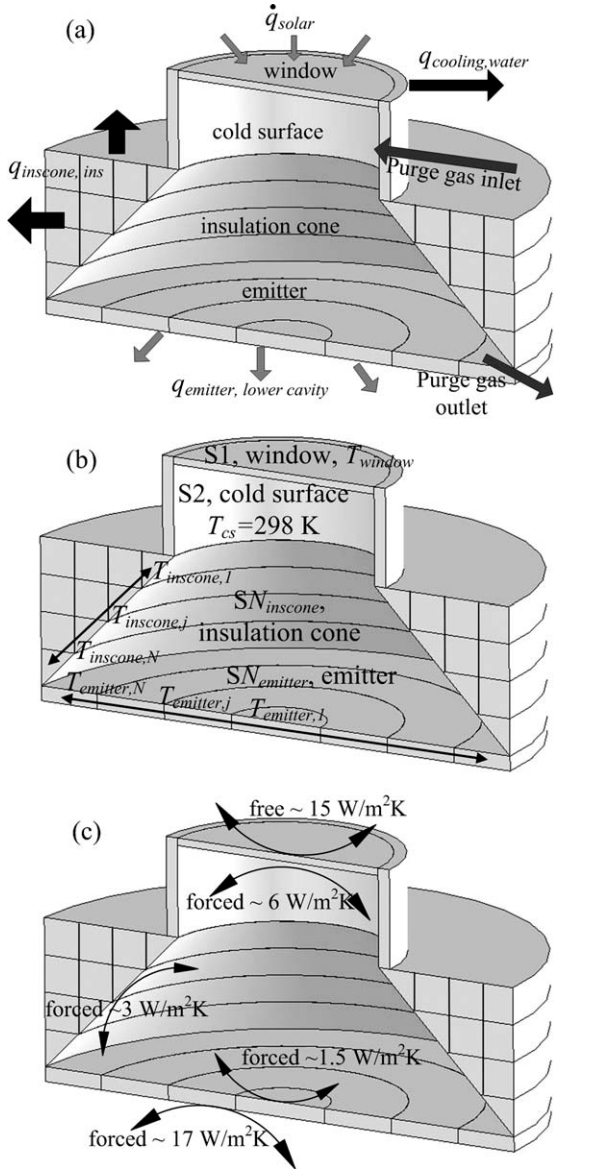

Figure 3. Schematic of the modeled reactor upper cavity: (a) heat transfer; (b) surfaces considered in radiative exchange; and (c) convective heat-transfer coefficients.

Table 2. Spectral Hemispherical Properties of the Quartz Window

Spectral Band	0–0.17 μm	0.17–3.5 μm	3.5 to ∞ μm
E	0.906	0.028	0.866
V	0.0	0.835	0.0
R	0.094	0.136	0.134

successive iteration steps. $q_{l,k,b}$ is zero for opaque surfaces and is the spectral radiative flux leaving surface k, directed towards the environment outside the enclosure,

$$q_{l,k,b} = R_{k,b}q_{e,k} + \underbrace{\mathrm{FF}_{b,iT_k}E_{k,b}\sigma T_k^4 + V_{k,b}q_{i,k,b}}_{q_{\mathrm{rerad},b}} \tag{5}$$

with $q_{\mathrm{rerad},b}$ representing the re-radiation losses—self emission of the window and transmission of radiative energy incident on the interior surface of the window—from the upper cavity for spectral band b. The individual spectral band solutions of Eq. 2 are summed over all bands to determine the net flux.

$$q_k = \sum_{b=1}^{N_{\mathrm{band}}} q_{k,b} \tag{6}$$

The temperature of the window was determined from the unsteady energy balance that considers the net radiation on the window, determined from Eq. 2, and the various cooling modes,

$$\frac{dH_{\mathrm{window}}}{dt} = \big(q_1 - q_{\mathrm{conv,env}} - q_{\mathrm{conv,upper\ cavity}} - q_{\mathrm{cooling,water}}\big)A_{\mathrm{window}} \tag{7}$$

The temperature of the water-cooled "cold surface" is 298 K, imposing a very strong heat sink in the upper cavity: nearly 50% of the applied radiative power is lost there. The emitter plate (SN_{emitter}) couples the upper cavity to the lower cavity. It is modeled as gray-diffuse concentric rings with an total emissivity of 0.88 at a temperature $T_{\mathrm{emitter},j}$ determined for each ring element by:

$$\frac{dH_{\mathrm{emitter},j}}{dt} = (q_{\mathrm{upper\ cavity,emitter},j} + q_{\mathrm{lower\ cavity,emitter},j})A_{\mathrm{emitter},j} + \sum \dot{Q}_{\mathrm{cond},j} - \big(q_{\mathrm{conv,emitter,upper\ cavity}} + q_{\mathrm{conv,emitter,lower\ cavity}}\big)A_{\mathrm{emitter},j} \tag{8}$$

where $\sum \dot{Q}_{\mathrm{cond},j}$ represents radial conductive heat transfer and $q_{\mathrm{lower\ cavity,\ emitter},j}$ is the net radiative flux on the surface of the emitter plate facing the lower cavity, obtained from the solution of the radiative exchange of the lower cavity (see Eq. 13). The surfaces of the insulation cone (SN_{inscone}) were modeled as gray-diffuse conical rings with an emissivity of 0.6 at $T_{\mathrm{inscone},j}$, determined through the transient energy balance considering 2D conduction and convective heat transfer,

$$\frac{dH_{\mathrm{inscone},j}}{dt} = \big(q_{\mathrm{inscone},j} - q_{\mathrm{conv,inscone}}\big)A_{\mathrm{inscone},j} + \sum \dot{Q}_{\mathrm{cond},j} \tag{9}$$

All upper cavity internal surfaces see forced convection heat transfer due to the purge gas flow. The window is additionally cooled by natural convection to the environment. Product gases at a temperature of the bed top surface $T_{\mathrm{bed,top}}$ contribute to forced convection on the emitter plate from the lower cavity side. Forced convective heat transfer on the window and emitter plate was calculated with the Nusselt correlation for a flow over a flat plate,[35]

$$Nu = \frac{hL_c}{k} = 0.664\, Re_{L_c}^{0.5} Pr^{1/3} \tag{10}$$

using window and emitter plate diameters as the characteristic dimensions L_c. Forced convective heat transfer affecting the insulating cone was modeled as developing laminar flow in a duct with mean diameter $\overline{D}$ and length $L_{\mathrm{upper\ cavity}}$,[35]

$$Nu = 3.66 + \frac{0.065\left(\overline{D}\Big/L_{\mathrm{upper\ cavity}}\right)Re\ Pr}{1 + 0.04\left[\left(\overline{D}\Big/L_{\mathrm{upper\ cavity}}\right)Re\ Pr\right]^{2/3}} \tag{11}$$

Heat transfer coefficients were determined in the range 6–4 W/m^{2}K for the window, 2–1.5 W/m^{2}K for the insulating ring, and 1.8–0.6 W/m^{2}K for the emitter plate. Finally, the solar absorption efficiency of the upper cavity is defined as:

$$\eta_{\mathrm{upper\ cavity}} = 1 - \frac{q_{l,1}}{q_{\mathrm{solar}}} \tag{12}$$

Lower cavity model

The lower cavity contains the reacting packed bed, which is coupled to the upper cavity by means of the common emitter plate ring elements. A detailed quasi-1D heat transfer model was previously formulated[21]—the main points of which are summarized here. The radiative flux q_j between the emitter plate ring elements, exposed SiC tiles, and the bed surface was solved with the radiosity formulation for a packed bed that shrank:

$$\sum_{j=1}^{N_{\mathrm{lower\ cavity}}} \left(\frac{\delta_{kj}}{\varepsilon_j} - F_{k-j}\frac{1-\varepsilon_j}{\varepsilon_j}\right)q_j = \sum_{j=1}^{N_{\mathrm{lower\ cavity}}} F_{k-j}\sigma(T_k^4 - T_j^4) \quad \text{for } k = 1\ldots N_{\mathrm{lower\ cavity}} \tag{13}$$

Effective conductive heat transfer $\dot{Q}_{\mathrm{cond},y}$ in the axial direction within the packed bed made use of an experimentally verified effective thermal conductivity k_{eff}, which coupled conductive, convective, and radiative heat transfer modes.[21,23] Additionally, heat transfer between the SiC tiles and the packed bed was handled by the term $\dot{Q}_{\mathrm{tile,bed}}$, considering the temperature at the interface. The 1D unsteady energy conservation equation on the packed bed is:

$$m_{\mathrm{feedstock}}Cp_{\mathrm{eff}}\frac{dT_{\mathrm{bed}}}{dt} = \dot{Q}_{\mathrm{cond},y} - \frac{dm_c}{dt}\Delta h_{\mathrm{chem}}(T_{\mathrm{bed}}) + \dot{Q}_{\mathrm{tile,bed}} \tag{14}$$

Equation 14 was solved with the fully implicit finite volume (FV) technique.[36] The reaction rate $\frac{dm_c}{dt}$ was expressed based on the sum of first order reactions of N pseudo-components[28]:

$$\frac{dm_c}{dt} = \sum_{j=1}^{N} m_{c,\mathrm{initial},j}k_j'(1 - X_j) \tag{15}$$

where the conversion $X_j = x_j\ (T,t)/x_{t=\infty,j}$ and $x_j(T,t)$ denotes the mass fraction of pseudo-component j having reacted until temperature T and time t, and $x_{t=\infty,j}$ is the total mass fraction of pseudo-component j reacted at time $t = \infty$. $k_j^{'}$ is assumed to obey the Arrhenius law, with apparent activation energies and frequency factors experimentally obtained by thermogravimetric measurements.[28] The bed shrink rate is expressed as:

$$\frac{dy}{dt} = \frac{1}{\rho_{\text{eff}} A_{\text{bed}}} \frac{dm_c}{dt} \tag{16}$$

Changes in the particle sizes, density, and porosity were considered within the gasification regime for scrap tire powder.[29] Because of the relatively high thermal conductivity of the SiC tiles (~25 W/mK), heat conduction through the SiC tiles was an important factor in delivering heat to deeper regions of the packed bed. The SiC tile temperatures were determined using a 1D finite volume grid that considered heat transport by conduction in the SiC tiles, heat exchange with the packed bed, heat exchange with the insulation, and the grid size changes associated with the packed bed shrink rate:

$$m_{\text{tile}} Cp_{\text{tile}} \frac{dT_{\text{tile}}}{dt} = \dot{Q}_{\text{cond},y} - \dot{Q}_{\text{tile,bed}} - \dot{Q}_{\text{tile,ins}} - H_{\text{tile}} \frac{dy}{dt} \tag{17}$$

The 1D bed assumption was justified by the observation of a flat bed top surface after each experimental run.[21] This assumption was verified by solving a two-dimensional packed bed thermal model using a fully implicit FV technique in cylindrical coordinates, resulting in nearly flat radial temperature profiles. CFD simulations in CFX of gas flow through porous media were conducted to support the assumption of a constant steam concentration required by the reaction rate expressions used in Eq. 14. The pressure drop across the porous packed-bed is given by[37]:

$$\nabla P = -\frac{\mu}{K_{\text{perm}}} \vec{W} + F_s \left|\vec{W}\right| W \tag{18}$$

with the permeability K_{perm} and Dupuit-Forchheimer coefficient F_s determined from the particle size and bed porosity using the Ergun equation,[38]

$$\nabla P = -\underbrace{\left(\frac{150(1-\phi)^2}{d_p^2 \phi^3}\right)}_{1/K_{\text{perm}}} \mu W - \underbrace{\left(\frac{1.75(1-\phi)\rho}{d_p \phi^3}\right)}_{F_s} W^2 \tag{19}$$

Water vapor mass fraction and stream lines for a steam-Ar flow through a representative porous packed bed are shown in Figure 4 (a 1/4 slice is shown), for a flow of 2 l_N/min Ar and 4 ml/min liquid water in a 14.3-cm-diameter packed bed of representative particles ($d_p \cong 2$ mm, $\phi \cong 0.56$, $\rho \cong 0.6$ kg/m^3). The stream lines show a strong radial distribution away from the inlet and are uniformly spaced at the height of the outlet indicating that the strengths of advection to diffusion are comparable (Peclet number = 1). The water vapor distribution is uniform along the radius of the packed bed at regions at and above the inlet which justifies the 1D assumption.

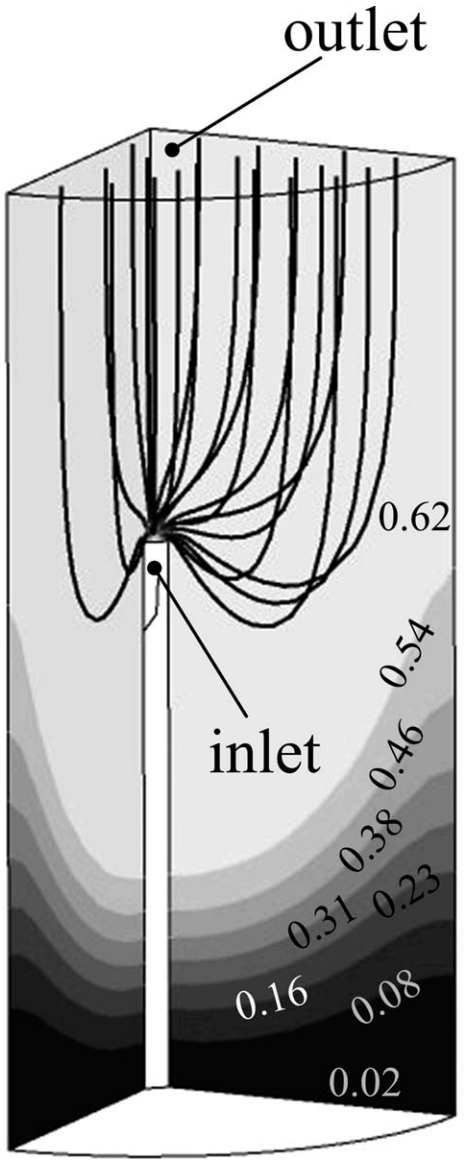

Figure 4. Water vapor mass fraction and stream lines for a steam-Ar flow through the porous packed bed.

Insulation model

The insulation exchanges heat by conduction with the upper and lower cavities and by convection with the environment. The 2D energy equation is given by Eq. 20 and solved using a fully implicit FV technique.[36]

$$\frac{dH}{dt} = \frac{1}{r}\frac{\partial}{\partial r}\left(kr\frac{\partial T}{\partial r}\right) + \frac{\partial}{\partial y}\left(k\frac{\partial T}{\partial y}\right) + S \tag{20}$$

where S is a volumetric source/sink and includes the thermal exchange with the environment, cooling water and/or wall tile components. Natural convection heat transfer to the environment was calculated for local heat transfer coefficients using Nusselt correlations[35]

$$\text{for vertical plate}: \; Nu = \left\{ 0.825 + \frac{0.387\, Ra_{L_c}^{1/6}}{\left[1 + \left(0.492/Pr\right)^{9/16}\right]^{8/27}} \right\} \tag{21}$$

$$\text{for horizontal plate (hot surface facing up)}: \; Nu = 0.54 Ra_{L_c}^{1/4} \tag{22}$$

$$\text{for horizontal plate (hot surface facing down)}: \; Nu = 0.27 Ra_{L_c}^{1/4} \tag{23}$$

with L_c being determined for each surface grid element based on the ratio of surface area to perimeter. Heat transfer coefficients were in the 1–2 W/m^{2}K range. Water cooling affecting the reactor front was modeled as an internal forced turbulent flow of water in a duct with an L_c as the hydraulic diameter D_h with the Nusselt correlation,[35,39]

$$Nu = \frac{(f/8)(Re_{L_c} - 1000)\,\mathrm{Pr}}{1 + 12.7(f/8)^{0.5}\left(\mathrm{Pr}^{2/3} - 1\right)} \tag{24}$$

where f is the friction factor with roughness values taken for new stainless steel,

$$\frac{1}{f^{1/2}} \cong -1.8 log \left[\frac{6.9}{Re_{L_c}} + \left(\frac{\varepsilon_r / D_h}{3.7} \right)^{1.11} \right] \tag{25}$$

Model Validation and Discussion

Figure 5 shows the applied solar radiative flux and the resulting experimentally measured and numerically modeled temperatures for the steam gasification of the three waste feedstocks investigated. The overall matching of the modeled and measured temperature profiles is good. The dynamics of the measured and modeled $T_{\text{upper cavity}}$ agree quite well in the heating phase under rather different irradiation conditions. It must be noted that the significant discrepancy between the measured and modeled $T_{\text{upper cavity}}$ in Figure 5b stems presumably from direct irradiation of the thermocouple during the experiment. In Figure 5c, the lower measured temperatures stem from the melting of ash deposits on the bed top surface which imposed strong heat sinks not considered in the model. Changes in particle size and porosity during the reaction were considered in the gasification regime for scrap tire powder but not for the other two feedstocks. These physical changes, particularly in the strongly represented pyrolytic regimes, may play an important role.

The model appears to replicate well the onset of important endothermic reactions above 1000 K for materials with large fixed carbon fractions. This is seen in Figure 5a and is characterized by a flattening of the curve of $T_{\text{lower cavity, bottom}}$ for scrap tire with 27.7% fixed carbon. Correspondingly, industrial and sewage sludge (Figure 5b,c), with their very low fixed carbon fractions experience a less important endothermic heat sink and lower reaction rates within the gasification temperature range however are affected by slow bed shrink rates and large ash deposits which impose a temperature flattening for the modeled profiles.

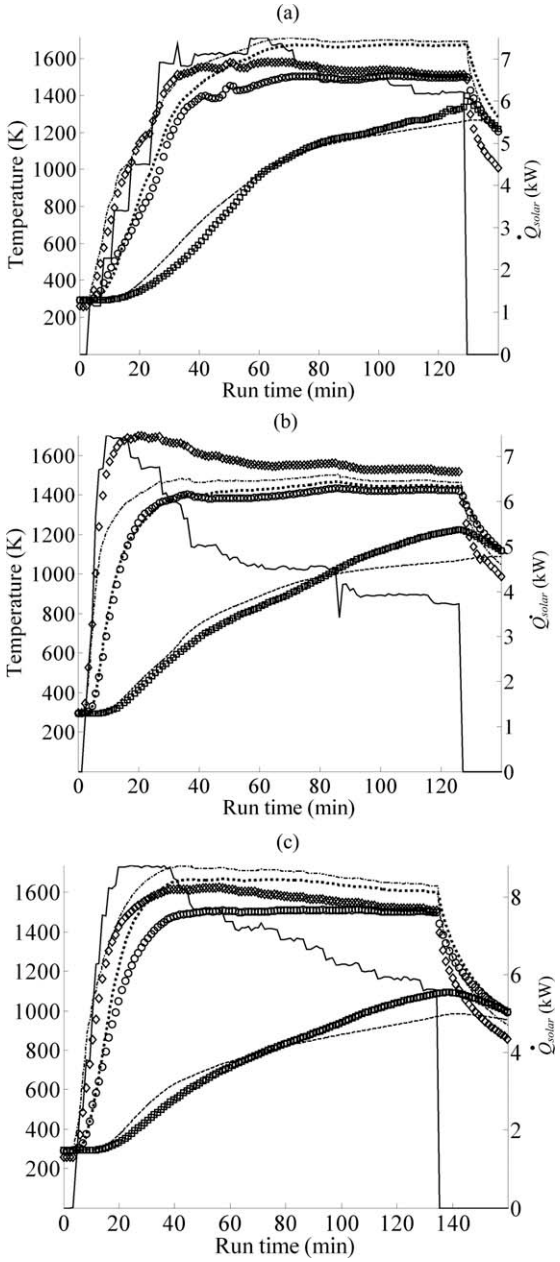

Figure 5. Experimentally measured and numerically simulated temperatures under variable radiative power inputs for the solar steam-gasification of: (a) scrap tire powder, (b) industrial sludge, and (c) sewage sludge.

◇, $T_{\text{upper cavity}}$ (exp); ○, $T_{\text{lower cavity, top}}$ (exp); □, $T_{\text{lower cavity, bottom}}$(exp); ▬■, $T_{\text{upper cavity}}$(model); ■■, $T_{\text{lower cavity, top}}$(model); --, $T_{\text{lower cavity, bottom}}$(model); ▬, $\dot{Q}_{\text{solar}}$

Figure 6 shows modeled reaction and bed shrink rates. All three waste feedstocks show high reaction rates associated with volatile release at the beginning of the run below 900 K. Above 1000 K, the gasification of only small quantities of fixed carbon produces a significant reduction in reaction

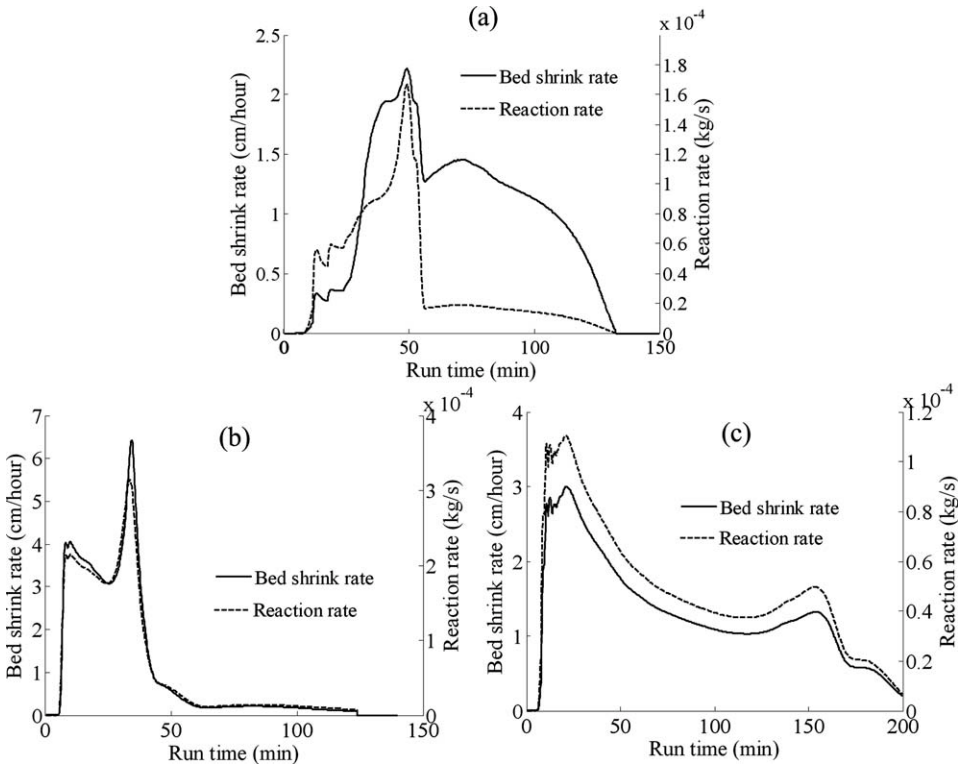

Figure 6. Simulated reaction rates and bed shrink rates for the solar steam-gasification of: (a) scrap tire powder, (b) industrial sludge, and (c) sewage sludge.

rate. Due to varying density and porosity for scrap tire powder, the bed shrink rate deviates from the reaction rate, as observed in Figure 6a.

Power partitioning for the steam-gasification of sewage sludge is shown in Figure 7 for the irradiation period. The energy going to heat the feedstock and power the reaction is on the order of 15% of the input solar power. Power associated with environmental losses corresponds to thermal losses to the water-cooled steel reactor front as well as free convection on external surface. As expected, the principal mode of heat loss is the radiative heat transfer to the cold surface; underlining the importance of eliminating any such potential heat sinks from the high-flux regions in the upper cavity.

The solar absorption efficiency (Eq. 12) and the temperatures of the upper cavity and window are shown in Figure 8 for the solar steam-gasification of sewage sludge. At the beginning of the run, the upper cavity is strongly influenced by the nonzero reflectance of the window. Thereafter, an increase in reradiation from the upper cavity and window self-emission lead to a further decrease in retained radiative energy.

The solar upgrade factor U and the solar-to-fuel energy conversion efficiency $\eta_{\text{solar-to-fuel}}$ are defined as:

$$U = \frac{m_{\text{syngas}} \cdot \text{LHV}_{\text{syngas}}}{m_{\text{feedstock}} \cdot \text{LHV}_{\text{feedstock}}} \tag{26}$$

$$\eta_{\text{solar-to-fuel}} = \frac{m_{\text{syngas}} \cdot \text{LHV}_{\text{syngas}}}{Q_{\text{solar}} + m_{\text{feedstock}} \cdot \text{LHV}_{\text{feedstock}}} \tag{27}$$

where Q_{solar} is the total solar energy delivered to the outer surface of the window over the duration of the experimental run, $m_{\text{feedstock}}$ is the converted feedstock mass, and m_{syngas} is the evolved syngas mass. Note that $\eta_{\text{solar-to-fuel}}$ takes into account the energy input of both solar and calorific content of feedstock, while U refers to the solar energy stored in the syngas product. For the model, the syngas is assumed to have the equilibrium composition at the temperature of the individual bed volumes integrated over the duration of the experimental run. As devolatilization is not an equilibrium process, intermediate pyrolytic products (tars, oils, C-2, and higher hydrocarbon gases) are

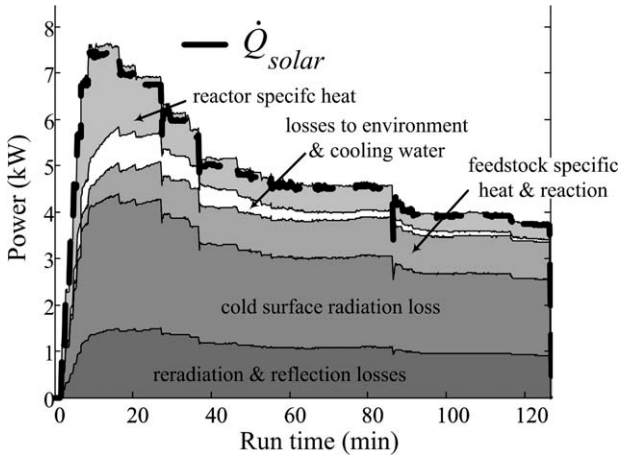

Figure 7. Power partitioning and applied input solar power during the steam-gasification of industrial sludge.

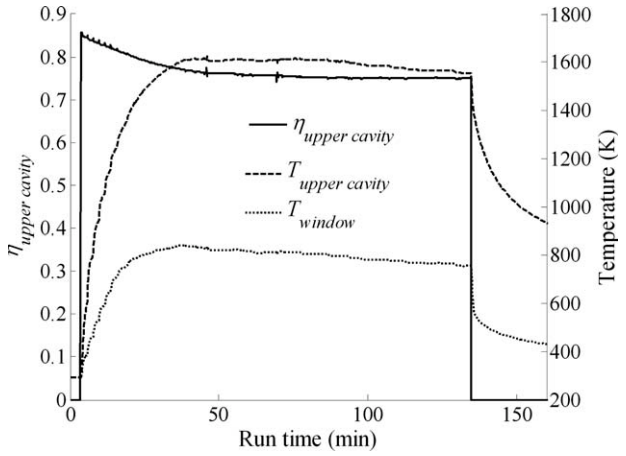

Figure 8. Solar absorption efficiency and the temperatures of the upper cavity and window during for the solar steam-gasification of sewage sludge.

not considered in the useful products. Experimentally determined and numerically simulated $m_{\text{feedstock}}$, $\eta_{\text{solar-to-fuel}}$, and U are shown in Table 3. For scrap tire powder, deposits of oils and particles prevented closing the carbon balanced which negatively affected the experimentally determined $\eta_{\text{solar-to-fuel}}$ and U. The discrepancy in the measured and simulated U and $\eta_{\text{solar-to-fuel}}$ stems in part from not considering C-2 and higher hydrocarbon gases arising during pyrolysis. In the case of sewage sludge, the higher modeled temperatures automatically drove higher reaction rates which overestimated the reacted mass. Finally, the difficulty in describing highly heterogeneous, strongly devolatizing feedstocks imposed errors in the treatment of effective packed bed properties such as heat capacity and thermal conductivity.

Scale-Up to a 200-kW Solar Reactor

The reactor model was applied to analyze the performance of a 200-kW solar gasifier converting industrial sludge under the conditions of a simulated solar day consisting of a solar flux increase of 50 suns/min to 842 suns followed by an 8-h hold and 4-h cooling period. The fixed-bed reactor parameters are shown in Table 4, with the diameters of the lower and upper cavities as well as the packed bed made equal and varied between 1.5 and 4 m in 0.25 m steps. A 5-mm cold surface was retained in the upper cavity representing a water-cooled gasket necessary to seal the window.

Table 4. Simulation Parameters of the 200-kW Solar Reactor

Nominal power $\dot{Q}_{\text{solar}}$	200 kW
Upper cavity height (m)	0.65
Lower cavity height (m)	0.85
Aperture diameter (m)	0.55
Initial packed bed height (m)	0.5
Radial insulation thickness (m)	0.18
Axial insulation thickness (m)	0.18
Solar flux at aperture (Suns)	842
Cavity/packed bed diameter (m)	1.5–4.0

The impact of packed-bed diameter on $\eta_{\text{solar-to-fuel}}$, $T_{\text{bed,top}}$, and the specific syngas power are shown in Figure 9. With increasing bed diameters, the radiation flux decreases in the upper and lower cavities, resulting in a decrease in temperatures from 1850 K at 1.5 m diameter to 1300 K at the 4 m diameter. The size increase, however, exposes more material to these temperatures. Furthermore, thanks to the high volatile content (62.2%) of industrial sludge and negligible heat of reaction of devolatilization, 62.2% of the batch is effectively converted without an energy penalty, producing the strong increase in $\eta_{\text{solar-to-fuel}}$. The specific syngas power, defined as the average lower heating value of the product gas evolved per unit bed area and per unit time, decreases only slightly—from 49 to 39 kW/m^2—as the rate of the gasification reactions falls with lower reactor temperatures. As the fixed carbon fraction is only 12%, this effect is small. The steam gasification of industrial sludge achieves a peak efficiency of 89.4% at a 4 m diameter lower cavity.

Figure 10 shows the reaction rates and solar radiative power input for a simulated 12-h solar run of the 200-kW solar reactor with packed-bed diameters 1.5, 2, 2.5, and 3 m. Under the rapidly increasing solar flux, the reaction rate rises thanks to rapid low-temperature volatile release (<900 K).[28] As the bed temperatures pass into the gasification range, the reaction rates fall strongly owing to the low fixed carbon fraction. By virtue of larger bed surface areas, larger diameter reactors achieve higher reaction rates for the same radiative power, supporting higher efficiencies. Between the 1.5 and 3.0 m diameters, there is a 67% increase in the peak reaction rate during devolatilization and a doubling in the gasification driven range at the end of the solar day. There is no significant transient penalty in going to larger reactors due to the low temperatures required for devolatilization onset (<500 K) and the good insulation of the packed bed from the walls by virtue of its own poor thermal conductivity. Notably, during the 4-h cooling period, the latent heat of the reactor and hot feedstock supports the gasification reaction longer in larger reactors. Gas evolution can continue

Table 3. Experimental and Simulated Performance Indicators for the Solar Steam-Gasification of Carbonaceous Waste Feedstocks

	Scrap Tire Powder		Industrial Sludge		Sewage Sludge	
	Experimental	Modeled	Experimental	Modeled	Experimental	Modeled
$m_{\text{feedstock}}$ (kg)	0.263	0.294	0.423	0.507	0.488	0.595
U (−)	0.83	1.25	1.07	1.17	1.16	1.35
$\eta_{\text{solar-to-fuel}}$ (%)	17.3%	27.4%	28.0%	24.7%	18.0%	17.4%

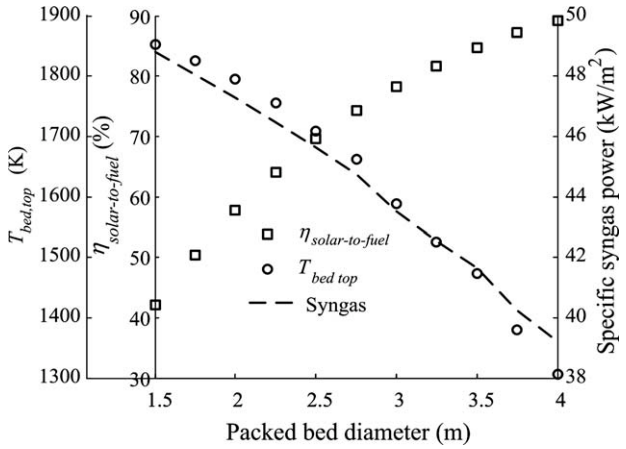

Figure 9. Solar-to-fuel energy conversion efficiency, specific syngas power, and top bed temperature as a function of the packed-bed diameter for a simulated 12-h solar run of the 200-kW solar reactor for steam-gasification of industrial sludge.

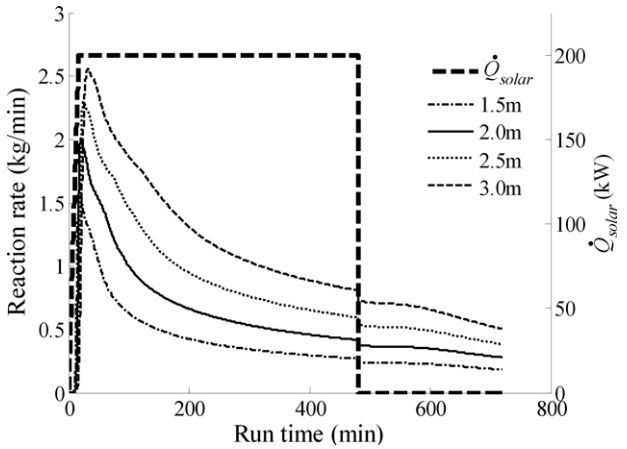

Figure 10. Reaction rates and radiative power for a simulated 12-h solar run of the 200-kW solar reactor for steam gasification of industrial sludge.

even at lower temperatures because of the large volatile content. As shown with the 8 kW prototype,[19] it is possible to convert—through cracking or gasification—evolved tars as they pass through the high-temperature regions at the top of the bed and undergo thermal decomposition. The longer residence times in the deeper packed bed at the pilot scale are favorable for their conversion. It must also be noted that the reaction rates of industrial sludge as shown for this batch configuration are undesirable for an industrial facility as they require sizing equipment to handle large peaks in production rates which occur for only a fraction of the time.

The power partitioning is shown in Figure 11 for reactors with packed bed diameters 2 and 4 m during a simulated 12-h solar run. For the larger packed bed, a larger portion of solar power input is consumed by the sensible heat of the reactor; however, more heat is delivered to the reacting packed bed by virtue of proportionally greater packed-bed surface to reactor surface. Similarly, larger reactors lose less energy by reradiation due to lower upper cavity temperatures. Notably, heat losses to the environment, cooling water, and cold surfaces remain nearly constant despite larger external surface areas because of the good insulation and a decrease in reactor inner temperatures. The above effects lead to higher overall $\eta_{\text{solar-to-fuel}}$.

Conclusions

A dynamic model for a solar-driven packed-bed reactor has been developed for the steam gasification of heterogeneous, high-volatile content, carbonaceous waste feedstocks. The boundary condition to the model is the applied solar flux, which makes the model suitable for dynamic simulations under transient solar irradiation conditions. Simulation of the upper cavity considered radiative exchange in a windowed enclosure containing the emitter plate which thermally couples the upper and lower cavities as well as heat transfer to the reactor insulation. A previously developed quasi-1D model is used for the lower cavity containing the packed bed, which couples the rate of heat transfer to the rate of the gasification reaction. Reaction rates considered pyrolysis and gasification with enthalpies

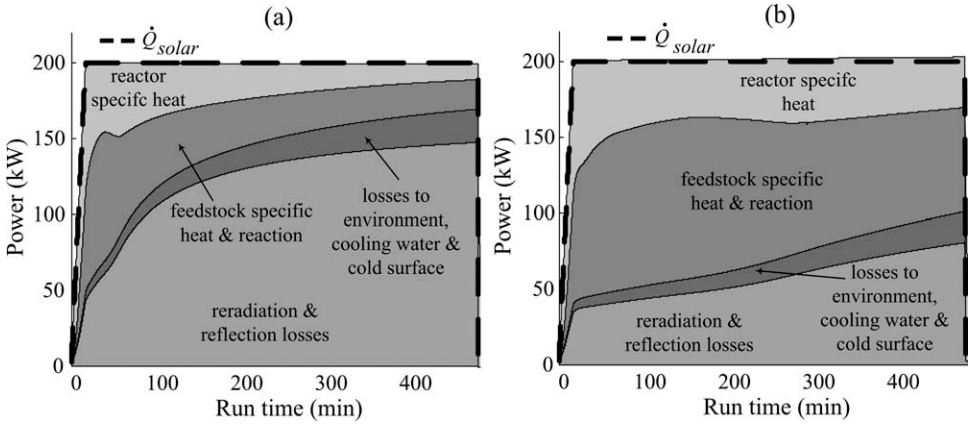

Figure 11. Power partitioning for a simulated 12-h solar run for the steam gasification of industrial sludge in a 200-kW solar reactor with packed bed diameters: (a) 2 m and (b) 4 m.

of reaction determined from equilibrium compositions of steam-feedstock systems. A 2D heat transfer model was applied to the reactor insulation which interacts with the environment. The model was validated with experimental data using an 8-kW reactor prototype for the steam gasification of scrap tire powder and industrial and sewage sludges in terms of reactor temperatures, converted mass, energy conversion efficiency, and upgrade factor. The model was further applied to analyze a 200-kW solar gasifier of industrial sludge operating under a simulated solar day. Larger packed-bed diameters were found to convert more material with the same solar input by virtue of lower reradiation losses and a greater portion of applied heat delivered to the reacting packed bed. Solar-to-fuel energy conversion efficiencies of up to 89.4% were determined for industrial sludge with a reactor having a 4 m diameter packed bed.

Acknowledgments

The authors thank C. Wieckert, P. von Zedtwitz, and the technical staff at the Paul Scherrer Institute for the experimental data collected at PSI's High-Flux Solar Simulator.

Notation

δ_{kj} = Kronecker function ($\delta_{ij} = 1$ for $i = j$; $\delta_{ij} = 0$ for $i \neq j$)
ε = surface emissivity
ε_r = relative roughness
ρ = density, kg/m^3
σ = Stephan-Bolzmann constant, W/m^{2}K^4
μ = viscosity, kg/ms
ϕ = porosity
η = energy conversion efficiency, %
A = surface area, m^2
Cp = specific heat capacity, J/kgK
$\overline{D}$ = mean diameter, m
D_h = hydraulic diameter, m
d_p = particle diameter, m
E = hemispherical emittance
f = friction factor
$F_{k\text{-}j}$ = view factor from surface k to j
$FF_{\lambda T}$ = fractional function
F_s = quadratic loss coefficient, kg/m^4
Δh_{chem} = specific enthalpy change of reaction, J/kg
H = enthalpy, J
h = convective heat transfer coefficient, W/m^{2}K
k = thermal conductivity, W/mK
K_{perm} = permeability constant, m^2
L_c = characteristic dimension, m
LHV = lower heating value, kJ/kg
m = mass, kg
N = number of discrete units
Nu = Nusselt number
Pr = Pradlt number
P = pressure, Pa
$\dot{Q}$ = power, W
Q = energy, J
q = flux, W/m^2
r = radius, m
R = hemispherical reflectance
Ra = Rayleigh number
Re = Reynolds number
S = volumetric heat source/sink, W/m^3
SN = surface number
t = time, s
T = temperature, K
U = upgrade
V = hemispherical transmittance
W = velocity, m/s
$\overline{W}$ = mean velocity, m/s
X = conversion
x = mass fraction
y = axial direction

Subscripts

λ = wavelength, μm
b = spectral band index
band = spectral band
bed = packed bed
bottom = bottom
c = carbonaceous
cooling = active cooling
cond = conduction
conv = convection
cs = cold surface
e = External
eff = Effective
emitter = emitter plate
env = environment, T = 292K
feedstock = Feedstock
free = free convection
forced = forced convection
i = Incident
initial = initial condition
j,k = general indices
inscone = insulation cone
ins = bulk insulation
l = leaving
lower cavity = lower cavity
o = radiosity
rerad = reradiation
syngas = syngas
solar = solar radiation
solar-to-fuel = solar to chemical fuel energy conversion
tile = tiles
top = top surface
upper cavity = upper cavity
water = water
window = window

Superscripts

new = new iteration value
old = old iteration value

Literature Cited

1. Steinfeld A, Palumbo R. Solar Thermochemical Process Technology. In: Meyers RA, editor. *Encyclopedia of Physical Science and Technology*. London: Academic Press, 2001:237–256.
2. Piatkowski N, Wieckert C, Weimer A, Steinfeld A. Solar driven steam gasification of carbonaceous feedstocks –a review. *Energy Environ Sci*., 2011;4:73–82.
3. Higman C, van der Burgt M. *Gasification*. Burlington: Elsevier Science, 2008.
4. von Zedwitz P, Steinfeld A. The solar thermal gasification of coal—energy conversion efficiency and CO_2 mitigation potential. *Energy*. 2003;28:441–456.
5. Morris M, Waldheim L. Energy recovery from solid waste fuels using advanced gasification technology. *Waste Manage*. 1998;18:557–564.
6. Filippis PD, Borgianni C, Paolucci M, Pochetti R. Prediction of syngas quality for two-stage gasification of selected waste feedstocks. *Waste Manage*. 2004;24:633–639.
7. Senneca O, Chirone R, Masi S, Salatino P. A thermogravimetric study of nonfossil solid fuels. 1. Inert pyrolysis. *Energy Fuels*. 2002;16:653–660.
8. Malkow T. Novel and innovative pyrolysis and gasification technologies for energy efficient and environmentally sound MSW disposal. *Waste Manage*. 2004;24:53–79.
9. Gregg DW, Aiman WR, Otsuki HH, Thorsness CB. Solar coal gasification. *Solar Energy*. 1980;24:313–321.
10. Trommer D, Noembrini F, Fasciana M, Rodriguez D, Morales A, Romero M, Steinfeld A. Hydrogen production by steam-gasification of

petroleum coke using concentrated solar power—I. Thermodynamic and kinetic analyses. *Int J Hydrogen Energy*. 2005;30:605–618.
11. Mueller R, Von Zedtwitz P, Wokaun A, Steinfeld A. Kinetic investigation on steam gasification of charcoal under direct high-flux irradiation. *Chem Eng Sci*. 2003;58:5111–5119.
12. Z'Graggen A, Haueter P, Trommer D, Romero M, de Jesus JC, Steinfeld A. Hydrogen production by steam-gasification of petroleum coke using concentrated solar power—II. Reactor design, testing and modeling. *Int J Hydrogen Energy*. 2006;31:797–811.
13. Von Zedwitz P, Steinfeld A. Steam gasification of coal in a fluidized-bed/packed-bed reactor exposed to concentrated thermal radiation—modeling and experimental validation. *Ind Eng Chem Res*. 2005;44:3852–3861.
14. Z'Graggen A, Haueter P, Maag G, Vidal A, Romero M, Steinfeld A. Hydrogen production by steam-gasification of petroleum coke using concentrated solar power—III. Reactor experimentation with slurry feeding. *Int J Hydrogen Energy*. 2007;32:992–996.
15. Van Heek KH. General aspects and engineering principles for technical application of coal gasification. In: Figueiredo, JL, editor. Carbon and Coal Gasification, NATO ASI Series. Dordercht: Kluwer, 1986.
16. Gregg DW, Taylor RW, Campbell JH, Taylor JR, Cotton A. Solar gasification of coal, activated carbon, coke and coal and biomass mixtures. *Solar Energy*. 1980;25:353–364.
17. Flechsenhar M, Sasse C. Solar gasification of biomass using oil shale and coal as candidate materials. *Energy*. 1995;8:803–810.
18. Schaffner B, Meier A, Wuillemin D, Hoffelner W, Steinfeld A. Recycling of hazardous solid waste material using high-temperature solar process heat—II. Reactor design and experimentation. *Environmental science and technology*. 2003;37:165–170.
19. Piatkowski N, Wieckert C, Steinfeld A. Experimental investigation of a packed-bed solar reactor for the steam-gasification of carbonaceous feedstocks. *Fuel Process Technol*. 2009;90:360–366.
20. Nipattummakul N, Ahmed I, Kerdsuwan S, Gupta AK. High temperature steam gasification of wastewater sludge. *Appl Energy*. 2010;87:3729–3734.
21. Piatkowski N, Steinfeld A. Solar driven coal gasification in a thermally irradiated packed bed reactor. *Energy Fuels*. 2008;22: 2043–2052.
22. Lipinski W, Steinfeld A. Heterogeneous thermochemical decomposition under direct irradiation. *Int J Heat Mass Transfer*. 2004; 47:1907–1916.
23. Osinga T, Olalde G, Steinfeld A. Solar carbothermal reduction of ZnO: shrinking packed-bed reactor modeling and experimental validation. *Ind Eng Chem Res*. 2004: 43; 7981–7988.
24. Atkinson B, Merrick D. Mathematical models of the thermal decomposition of coal: 4. Heat transfer and temperature profiles in a coke-oven charge. *Fuel*. 1983;62:553–561.
25. Yogev A, Kribus A, Epstein M, Kogan A. Solar "tower reflector" systems: a new approach for high-temperature solar plants. *Int J Hydrogen Energy*. 1998;23:239–245.
26. Welford WT, Winston R. *High Collection Nonimaging Optics*. San Diego: Academic Press, 1989.
27. Petrasch J, Coray P, Meier A, Brack M, Haeberling P, Wuillemin D, Steinfeld A. A 50-kW 11,000-suns novel high-flux solar simulator based on an array of Xenon arc lamps. *J Solar Energy Eng*. 2007;129:405–411.
28. Piatkowski N, Steinfeld A. Reaction kinetics of the combined pyrolysis and steam-gasification of carbonaceous waste materials. *Fuel*. 2010;89:1133–1140.
29. Haussener S, Lipinski W, Wyss P, Steinfeld A. Tomography-based analysis of radiative transfer in reacting packed beds undergoing a solid-gas thermochemical transformation. *ASME J Heat Transf*. 2010;132:061201–1/7.
30. Lopez-Peinado AJ, Tromp PJJ, Moulijn JA. Quantitative heat effects associated with pyrolysis of coals, ranging from anthracite to lignite. *Fuel*. 1989;68:999–1004.
31. Müller R, Lipinski W, Steinfeld A. Transient heat transfer in a directly-irradiated solar chemical reactor for the thermal dissociation of ZnO. *Appl Therm Eng*. 2008;28:524–531.
32. Müller R, Steinfeld A. Band-Approximated Radiative Heat Transfer analysis of a solar chemical reactor for the thermal dissociation of zinc oxide. *Solar Energy*. 2007;81:1285–1294.
33. Maag G, Falter C, Steinfeld A. Temperature of a quartz/sapphire window in a solar cavity-receiver. *ASME J Solar Energy Eng*., 2011;133:1–4.
34. Siegel R, Howell JR. *Thermal Radiation Heat Transfer*, 4th ed. Washington: Taylor and Francis-Hemisphere, 2001.
35. Çengel YA. *Heat Transfer*. New York: McGraw Hill, 2003.
36. Patankar SV. *Numerical Heat Transfer and Fluid Flow*. New York: Taylor and Francis, 1980.
37. Bejan A, Nield DA. *Convection in Porous Media*. New York: Springer, 2006.
38. Ergun S. Fluid flow through packed columns. *Chem Eng Prog*. 1952;48:89–94.
39. White FM. *Fluid Mechanics*. New York: McGraw Hill, 2003.

Manuscript received Sept. 14, 2010, revision received Nov. 16, 2010, and final revision received Jan. 4, 2011.